



## Multiscale modeling of lithium-ion battery electrodes based on nano-scale X-ray computed tomography



Ali Ghorbani Kashkooli <sup>a</sup>, Siamak Farhad <sup>b,\*</sup>, Dong Un Lee <sup>a</sup>, Kun Feng <sup>a</sup>, Shawn Litster <sup>c</sup>, Siddharth Komini Babu <sup>c</sup>, Likun Zhu <sup>d</sup>, Zhongwei Chen <sup>a,\*\*</sup>

<sup>a</sup> Department of Chemical Engineering, University of Waterloo, Waterloo, ON N2L 3G1, Canada

<sup>b</sup> Department of Mechanical Engineering, University of Akron, Akron, OH 44325-3903, United States

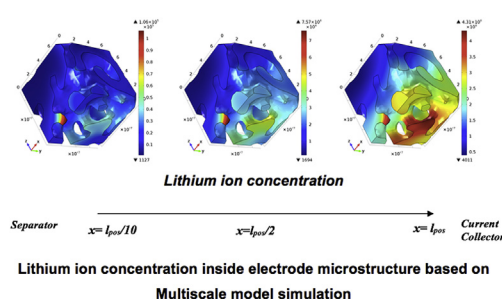
<sup>c</sup> Department of Mechanical Engineering, Carnegie Mellon University, Pittsburgh, PA 15213, United States

<sup>d</sup> Department of Mechanical Engineering, Indiana University Purdue University, Indianapolis, IN 46202, United States

### HIGHLIGHTS

- A multiscale model is developed to study lithium ion battery electrodes.
- The electrode microstructure is reconstructed based on X-ray computed tomography.
- The model predicts experimental data more accurately than the homogenous models.
- Inhomogeneity causes wider distribution of properties compared to homogenous models.
- The developed model is applicable to any lithium ion battery electrode material.

### GRAPHICAL ABSTRACT



### ARTICLE INFO

#### Article history:

Received 19 September 2015

Received in revised form

23 December 2015

Accepted 28 December 2015

Available online 14 January 2016

#### Keywords:

Lithium-ion battery

Inhomogeneous electrodes

Micro/nanostructure

Multiscale modeling

X-ray computed tomography

### ABSTRACT

A multiscale platform has been developed to model lithium ion battery (LIB) electrodes based on the real microstructure morphology. This multiscale framework consists of a microscale level where the electrode microstructure architecture is modeled and a macroscale level where discharge/charge is simulated. The coupling between two scales are performed in real time unlike using common surrogate based models for microscale. For microscale geometry 3D microstructure is reconstructed based on the nano-scale X-ray computed tomography data replacing typical computer generated microstructure. It is shown that this model can predict the experimental performance of LiFePO<sub>4</sub> (LFP) cathode at different discharge rates more accurate than the conventional homogenous models. The approach employed in this study provides valuable insight into the spatial distribution of lithium -ion inside the real microstructure of LIB electrodes. The inhomogenous microstructure of LFP causes a wider range of physical and electrochemical properties in microscale compared to homogenous models.

© 2016 Elsevier B.V. All rights reserved.

## 1. Introduction

Lithium-ion batteries (LIBs) have attracted a tremendous attention because of their high energy and power density compared to other electrochemical energy storage technologies.

\* Corresponding author.

\*\* Corresponding author.

E-mail addresses: [sfarhad@uakron.edu](mailto:sfarhad@uakron.edu) (S. Farhad), [zhwchen@uwaterloo.ca](mailto:zhwchen@uwaterloo.ca) (Z. Chen).

Recently, automotive industries have put considerable effort to accelerate electrification of vehicles using LIBs [1,2]. For this purpose, among different candidates for cathode material, LiFePO<sub>4</sub> (LFP) is believed to be promising choice due to its low price, superb safety, and enhanced rate capability [3–5]. In addition to material selection, the electrode architecture also plays a crucial role in improving the performance of LIBs [6,7]. The microstructure of LIB electrode remarkably influences the performance by providing certain interfacial surface area, lithium ion diffusion path, and active material connectivity [5,8], which particularly critical in automotive applications where the demands of energy and power densities are high [1].

The development of next generation high performance LIBs requires close relation between modeling and experiment. Mathematical models have been used to address physical and electrochemical processes occurring inside the battery and further employed to optimize electrode design. However, traditional models still relies on a simplified picture of homogenous electrode which do not provide sufficient information about the electrode's real microstructure. Newman and co-workers have developed one of the most successful LIB models based on the porous electrode and concentrated solution theory [9,10]. Newman's pseudo-2D (P2D) model assumes that the porous electrode is made of equally sized, isotropic, homogenous spherical particles [9]. This homogenous description of electrode structure results in smooth, uniform intercalation/de-intercalation of lithium inside the host materials and has proven to be successful in characterizing discharge/charge behaviors particularly at low to moderate rates [11,12]. Although P2D model assumptions are not preserved in real LIB porous electrodes, it is widely applied in a variety of LIB research due to its simplicity [13–15]. This includes the rate capability and design investigation [10,16] as well as thermal behavior [17–19] studies. However, it fails to predict the phenomena related to inhomogenous structure of the electrode microstructure such as performance drop at high rates [20,21]. In addition, the well-known method of estimating the specific surface area based on spherical particles and the electrode tortuosity using Bruggeman correction has been controversial [22,23]. Therefore, in order to have more genuine insight in LIBs research, there is a crucial need for an advanced model capable of simulating LIBs behavior based on the real electrode microstructure.

Recent advances in the X-ray computed tomography (XCT) have made nano-scale 3D microstructures capturing a reality. Nano-XCT offers the capability to non-destructively resolve the 3D structure of porous electrode as it provides high spatial resolution 2D stack to computationally reconstruct a 3D image of the electrode microstructure. The obtained 3D geometry could be an alternative to commonly used computer-generated geometries [20,24] in LIB 3D models. LIBs research involving XCT can be categorized into two general groups: the morphological studies and multiphysics modeling. The first group is dedicated to characterizing the 3D microstructure, particle distribution, pore scale morphological and transport properties analysis [22,25,26]. The second group, on the other hand, utilizes reconstructed 3D microstructure to simulate multiphysics phenomena occurring inside the cell such as discharge/charge performance [27], thermal behavior [28] and stress analysis [26]. Yan et al. [27] simulated the discharge behavior of LiCoO<sub>2</sub> (LCO) based on nano-XCT data. Their results show that the distributions of electrolyte concentration, current density, over potential and intercalation reaction rate are significantly different from the results obtained from the P2D model. Furthermore, the microstructure inhomogeneity is found to be responsible for the performance loss particularly at high discharge rates. Lim et al. [26] modeled diffusion-induced stress inside LCO particles which were reconstructed using XCT. Their results demonstrated that the

highest von Mises and Tresca stresses in a reconstructed particles are several times greater than those obtained from the simple spherical or ellipsoid particle with the same volume. Yan et al. [28] simulated the heat generation during galvanostatic discharge in LCO microstructure. Their results show that the simulation based on reconstructed microstructure predicts more heat generation than the P2D model at high discharge rates. The simulation based on the reconstructed microstructure commonly results in the wider distribution of physical and electrochemical properties. The authors attributed the higher predicted heat generation to this wider electrochemical properties distribution. Chung et al. [29] studied the electrochemical and chemo-mechanical response of LiMn<sub>2</sub>O<sub>4</sub> (LMO) cathodes based on the XCT method. Their simulations show that particle size polydispersity of microstructures impacts the local chemical and electrical behavior of a porous electrode.

In the present work, we aim to develop a model based on the real microstructure of the electrode. Among different candidates, LFP was chosen as the focused technology due to the aforementioned reasons. Applying the above mentioned method on the electrode with nano-particles, e.g. LFP, to study multiphysics phenomena, poses the inherent multiscale difficulty involved in the LIB research [30]. Models involve microstructure study LIBs behavior in two different length scales simultaneously; the first scale is in the range of the particle size which is couple of micrometers in case of LCO and LMO and tenth of nanometers for LFP. In this work, this scale is called “microscale” wherein electrode architecture is incorporated in the model. The second scale is in the range of the electrode thickness, typically 100 μm, where discharge/charge is characterized and here is called “macroscale”. For a micro-particle electrode, the model length scale is from 10<sup>-6</sup> to 10<sup>-2</sup> m considering both microscale and macroscale. However, the scale is from 10<sup>-8</sup> to 10<sup>-2</sup> m for a nano-size particles. Thus, comparing electrodes made of nano-particles and micro-particles, the difference between model length scale ranges is two orders of magnitudes bigger in case of electrode with nano-particles. This requires around 10<sup>6</sup> times more mesh elements in 3D that would burden a huge extra amount of computational cost on the model simulation. To avoid this, the concept of multiscale modeling has been employed to investigate LFP electrode behavior [30–33]. First, the electrode microstructure was reconstructed based on the nano-XCT data and the intercalation flux were obtained based on the simulation results on microscale. Then, the intercalation flux was exported to the macroscale to update the state variables such as electric potentials and species concentrations in macroscale. Finally, the intercalation flux is updated based on the recent updated variables and sent back to microscale domain [34]. In this study, linking between microscale and macroscale is accomplished through coupling of equations at two sub-scales simultaneously [34], meaning that all the governing equations are solved concurrently in two scales and state variables are transferred between them in real time. To couple sub-scale models, another approach reported in the literature is serial coupling [35]. In the serial coupling, a surrogate-based model is determined from the pre-processed simulation data carried out on the microscale. The surrogate model is obtained based on the numerical experiment performed on microscale. For this, a quasi-steady state simulation of the governing equation is performed based on an experiment design for the initial values of state variables. Then, to couple the two scales, database and look up table [36,37] approach is used to couple microscale with macroscale. Although using serial method diminishes computational time, it includes error due to uncertainty in fitting the empirical model to microstructural data. In addition, the assumption of quasi steady state in microscale is highly questionable in a mainly time dependent model.

The purpose of this study is to establish an advanced imaged-

based multiscale computational framework capable of modeling LIBs at various design and operating conditions. The results are presented for an LFP cathode scanned by a nano-XCT device and processed/reconstructed by a commercial software package (Simpleware, HO, Exeter, England). To achieve accurate results, concurrent multiscale model is implemented in Comsol Multiphysics® software.

## 2. Electrode structure reconstruction

The LFP sample used in this study is from a commercial LFP/graphite cell which was disassembled in an argon filled glove box ( $H_2O < 0.5$  ppm,  $O_2 < 0.5$  ppm). Since Aluminum current collector affect the XCT scan, it was detached from the electrode by soaking in 6 M KOH solution [27]. The sample was imaged using nano-XCT (UltraXRM-L200, Xradia Inc., Pleasanton, CA) at Carnegie Mellon University [38]. A high resolution scan of region of interest with 50 nm resolution (16 nm cubic voxels) and 16  $\mu m$  field of view was performed. A total of 990 tomograms were obtained by rotating the sample over  $180^\circ$  with 16 nm distance between slices. Then, the obtained 2D stack was segmented using thresholding technique to convert greyscale stack to binary stack. Eventually, 3D morphology of the LFP nano particles was reconstructed based on the 2D stack by commercial software ScanIP 7 (Simpleware, HO, Exeter, England).

Fig. 1a shows a 2D raw morphology of the electrode

microstructure based on a tomogram obtained from 2D stack after segmentation. Fig. 1b shows the reconstructed 3D microstructure of the electrode consists of cluster of particles and Fig. 1c represents the SEM image of electrode nano particles. In Fig. 1a and b, the black region consists of cluster of active material particles whereas white region includes pore, additives comprising polymer binder (PVDF) and conductive carbon material. Since X-ray is highly sensitive to the atomic number, low atomic number additive phases could not be captured with one run of imaging. To distinguish different phases, two modes of imaging are needed: absorption contrast which capture active material and Zernike phase contrast that detects active material along with solid phase additives. Details method of distinguishing various electrode regions can be found in Ref. [39]. In this work, additives are not considered separately from the active material because it is hard to clearly distinguish them from active material. Moreover, treating them as separate region provokes an excessive computational load. It is shown that if the weight percentage of active material is high, the carbon material and polymer binder are distributed randomly in the electrode [40]. The weight percentage of active material in the current electrode is 90 percent obtained by Thermogravimetric Analysis (TGA) [41]. Hence, we assumed that the carbon material is randomly distributed among the active material to provide electronic connectivity. For this, a growing region image processing algorithm was applied on the active material region to provide fusion of neighbors active material together. The obtained 3D reconstructed microstructure

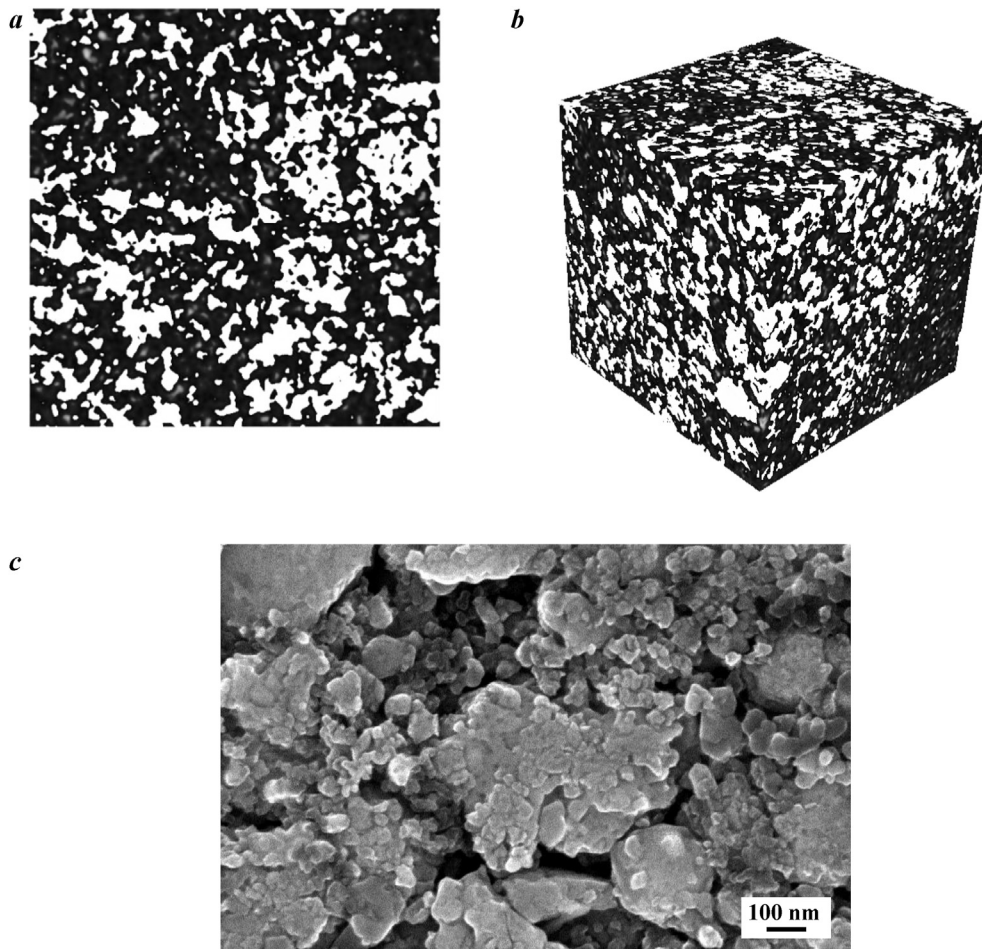


Fig. 1. Different morphological images of a commercial LFP (a) nano-XCT tomogram, 5  $\mu m$  each side (b) reconstructed structure, 5  $\mu m$  each side (c) SEM image, scale bar is 100 nm.

pore volume became 40% after filtering and image processing improvement which came in agreement with the 35% porosity of the real electrode obtained by Brunauer Emmett Teller (BET) measurement. The difference could be attributed to the unconnected pores which cannot be detected by BET. Video 1 displays the morphological evolution of the electrode microstructure during reconstruction after image processing.

Supplementary video related to this article can be found at <http://dx.doi.org/10.1016/j.jpowsour.2015.12.134>.

**3. Experiment**

For validation of the model, several coin cell (half-cells) were fabricated from the LFP cathode of the disassembled commercial LIB. Since LFP had been coated on both side of an aluminum sheet, the LFP coated on one side was removed using a cotton-based wipe soaked in 1-methyl-2 pyrolidinone (NMP) and scotch tape. To make the coin half-cells circular cathodes with area of 1.13 cm<sup>2</sup> were punched and coin cells (LIR2032-type) were assembled with a lithium metal foil as the counter electrode and an ion permeable separator (Celgard 2500). The electrolyte is 1 M lithium hexa-fluorophosphate (LiPF<sub>6</sub>) in 1:1 ethylene carbonate (EC): diethyl carbonate (DEC) and sealed before removal from the glove box. The cell then tested on a battery cycler (Neware CT-3008-5 V 10 mA). All cells were first cycled five times for the formation stage with a constant-current–constant-voltage CCCV protocol [42] on charge (CC at C/5 between 2.5 and 4.2 V and CV until  $I < C/25$ ) and a 30 min period of rest, followed by CC discharge between 4.2 and 2.5 V versus Li electrode. Then, in order to estimate the equilibrium potential, a fully charged electrode was discharged at CC at C/25 and the result is presented in Table 3. The rate-capability tests were accomplished on the coin half-cell setup by galvanostatic charge/discharge at C-rates ranging from C/25 to 4 C between 2.5 and 4.2 V versus Li electrode. For all rates, CCCV protocol was used for charge (CV until  $I < C/25$ ) to make sure the cathode came back to a fully charged state.

**4. Modeling and computer simulation**

Multiscale model development of the LIB half-cell based on the real microstructure is presented in this section. This includes the geometries and governing equations on 3D microscale and 1D macroscale domains along with the bridging between two scales. The microscale geometry is a Representative Elementary Volume (REV) of the total reconstructed electrode. The macro scale is a 1D sandwich model of Li foil | separator | cathode to simulate half-cell charge/discharge performance. As discussed in introduction, to couple the state variables such as electric potentials and species concentrations between two scales, concurrent approach is used. Bridging is accomplished through transferring the calculated intercalation flux on the macroscale as the boundary condition for microscale. Then, the governing equations in microscale is solved to update the lithium concentration inside microstructures and calculating the new intercalation flux. Next, the intercalation flux is sent back to the macroscale, which later be used in governing equations in macroscale domain to update state variables. The updated state variables in macroscale then is used to update intercalation flux which in the next time step would be applied as interfacial boundary condition in the microscale domain. This circular coupling, which is illustrated in Fig. 2, continues during the cell operation time. The coupling details will be further discussed in Section 4.3.

**4.1. Microstructure selection**

As discussed in the introduction, the reason that multiscale approach was chosen is due to the presence of LFP nano particles which creates complicated microstructure, see Fig. 1. In order to choose appropriate microstructure we apply the concept of Representative Elementary Volume (REV) which represents a portion of the electrode as a cluster of particles [43]. Majdabadi et al. [44] showed that the largest particle radius in the commercial LFP battery, which is similar to the one we disassembled, is around

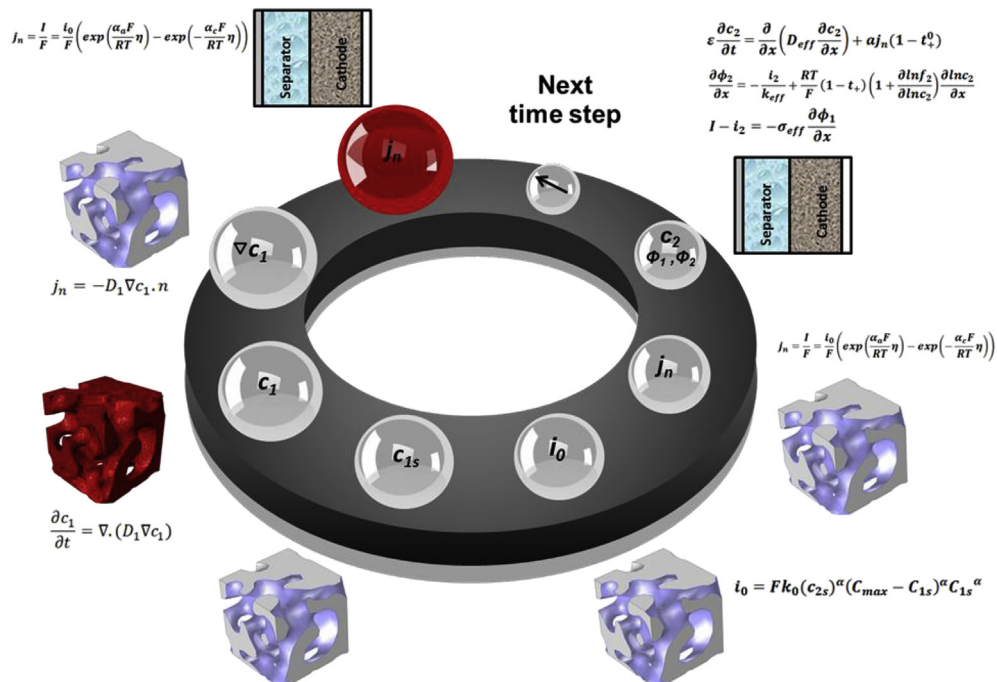


**Fig. 2.** Multiscale modeling framework.

169 nm. These size particles allocate around 10% (vol) of the active electrode material. Accordingly, we calculated the smallest volume of the electrode that has at least one particle with the largest size. We achieved a cubic REV with sides of 728 nm which is the largest characteristic size of the microstructure.

Another approach to find the smallest REV size is to calculate the electrode properties for a small cubic subdivision of the electrode sample. The subdivision size then will be increased until electrode properties e.g. porosity  $\epsilon$  and specific interfacial surface area per unit volume of electrode  $a$ , remain within an acceptable range. Table 1 shows porosity and specific surface area per unit volume for various cubic subdivisions using ScanIP 7 (Simpleware, HO, Exeter, England). As mentioned previously, the domain porosity is around 0.4. For the sizes above 707 nm, when the subdivision size increases, the porosity of the subdivisions remains within the 3% of the domain porosity. On the other hand, the average specific surface area of the electrode is around 3.6 (1/ $\mu\text{m}$ ) where it remains within the 9% of the domain specific surface area for the subdivisions above 707 nm.

Using the results of both approaches, a REV with 750 nm each side from reconstructed microstructure was chosen for the current simulation. Furthermore, mesh is also generated using ScanIP 7 (Simpleware, HO, Exeter, England), see Fig. S1.

#### 4.2. Governing equations in macroscale

In this subsection, the governing equations of mass and charge transfer are developed for each components of the 1D cell structure in macroscale, including the LFP porous cathode, a porous and ion permeable membrane separator, Li foil counter electrode, and the electrolyte that fills the cathode and separator pores. During discharge electron flows in the external circuit from lithium foil to the cathode current collector and lithium ion travels through separator to the cathode. The following electrochemical reaction happens during the discharge and charge process:

Positive Electrode:



Negative Electrode:



The mathematical model employed to simulate macroscopic 1D half-cell LIB is based on the porous electrode theory [45–47]. For the transport of lithium ion inside the electrolyte the concentrated solution theory is used which can be written as:

$$\epsilon \frac{\partial c_2}{\partial t} = \frac{\partial}{\partial x} \left( D_{eff} \frac{\partial c_2}{\partial x} \right) + a j_n (1 - t_+^0) \quad (3)$$

where  $c_2$  is the concentration of lithium inside electrolyte,  $D_{eff}$  is

effective diffusivity,  $j_n$  is the pore-solid flux of lithium ions, and  $t_+^0$  is the transference number of the lithium ion in the solution which is assumed to be constant in this work. The subscripts  $i = 1, 2$  are the solid and electrolyte phases, respectively, throughout this paper. The governing equations in macroscale is similar to the ones in P2D model. However, the model properties could be calculated using the real specific surface area,  $a$ , and the effective diffusivity,  $D_{eff}$  as described in Ref. [48].

The effective diffusivity is defined as [48]:

$$D_{eff} = D \frac{\epsilon}{\tau} \quad (4)$$

where  $D$  is the intrinsic diffusivity and  $\tau$  is the electrode tortuosity which accounts for the obstruction to diffusion by porous network. Generally, in traditional LIB modeling tortuosity is calculated using Bruggeman correlation [9,10,49]. However, Bruggeman derived the correlation for a specific structure containing spherical particles which is not the case for diverse morphology of LIB active materials [48]. In order to calculate the tortuosity, using heat and mass transfer analogy, the steady state conductive heat transfer was simulated on both pore network and active material microstructure. Video 2 displays the details of the mesh generated for the simulation inside active material microstructure (cube side is 1.5  $\mu\text{m}$ ). The temperature distribution was obtained within the pore network by applying temperature gradient in x, y, z directions separately (see Fig. S2 for result in y direction). To calculate the tortuosity, results obtained from the pore network must be compared to the one obtained through a uniform, non-porous sample with the same dimensions as discussed in Ref. [48] by cooper et al. Table 2 represents directional tortuosity and its average value based on the stationary heat transfer simulation. Electric potential in the solution  $\phi_2$  is represented by ohm's law as:

$$\frac{\partial \phi_2}{\partial x} = -\frac{i_2}{k_{eff}} + \frac{RT}{F} (1 - t_+) \left( 1 + \frac{\partial \ln f_2}{\partial \ln c_2} \right) \frac{\partial \ln c_2}{\partial x} \quad (5)$$

where  $i_2$  is current density in the electrolyte,  $k_{eff}$  is effective conductivity,  $R$  is the universal gas constant,  $T$  is temperature,  $F$  is Faraday's constant, and  $f_2$  is mean molar activity coefficient of electrolyte and is assumed to be constant. Since tortuosity is a geometric characteristics of the electrode, it is not related to the transport processes. Therefore,  $k_{eff}$  can also be calculated using eq. (4) by replacing diffusivity,  $D$  with conductivity,  $k$  using tortuosity values listed in Table 2. This is also valid for all upcoming effective parameters. The electric potential in the solid phase,  $\phi_1$ , is described using ohm's law in solid as follows:

$$I - i_2 = -\sigma_{eff} \frac{\partial \phi_1}{\partial x} \quad (6)$$

where,  $I$  is superficial current density,  $\sigma_{eff}$  is effective conductivity of solid matrix.

Supplementary video related to this article can be found at <http://dx.doi.org/10.1016/j.jpowsour.2015.12.134>.

The lithium ion intercalation reaction in the solid matrix is estimated from the Butler–Volmer equation as:

**Table 1**  
Porosity and specific surface area per unit volume for cubic subdivisions of the electrode sample with different size using ScanIP 7 (Simpleware, HO, Exeter, England).

Cube side (nm)	Porosity, $\epsilon$	Specific surface area, $a$ (1/ $\mu\text{m}$ )
2122	0.41	3.62
1415	0.36	3.59
1132	0.42	3.73
849	0.42	3.71
707	0.39	3.51
566	0.35	4.27
424	0.6	4.92
283	0.58	4.87

**Table 2**  
Directional tortuosity of both solid and electrolyte phase of the studied LFP cathode.

Region	Volume fraction	$\tau_x$	$\tau_y$	$\tau_z$	$\tau_{avg}$
Solid phase	0.6	1.6116	1.8154	1.7794	1.7311
Electrolyte phase	0.4	2.2544	2.4289	2.0844	2.2472

**Table 3**  
List of model parameters.

Parameter	Description	Value
A	Area of the electrode	1.13 cm <sup>2</sup>
$l_{pos}$	Positive electrode thickness	50 μm
$l_{sep}$	Separator thickness	52 μm
$\epsilon_{pos}$	Porosity of positive electrode	0.4
$\epsilon_{sep}$	Porosity of separator	1
$D_{LFP}$	Solid state binary diffusion coefficient of LFP	$7 \times 10^{-18}$ m <sup>2</sup> /s
$\sigma$	Electrical conductivity of positive electrode	0.03 S/m
$k_0$	Reaction rate constant in positive electrode	$2.5 \times 10^{-13}$ mol m <sup>-2</sup> s <sup>-1</sup> (mol m <sup>-3</sup> ) <sup>-1.5</sup>
$\alpha_a$	Anodic transfer coefficient	0.5
$\alpha_c$	Cathodic transfer coefficient	0.5
$i_f$	Exchange current density of lithium foil	19 A/m <sup>2</sup>
$c_{ini}$	Initial salt concentration in the electrolyte	1000 mol/m <sup>3</sup>
$c_{max}$	Maximum Lithium concentration in the LFP particles	22,800 mol/m <sup>3</sup>
$D_{LiPF_6}$	Salt diffusivity of electrolyte	$3 \times 10^{-10}$ m <sup>2</sup> /s
$t_+^0$	Lithium ion transference number	0.343
T	Cell Temperature	298 K
U	Open circuit potential of LFP	$U_{c/50} = 3.382 + 0.00470 y + 1.627 \exp(-81.163 y^{1.0138}) + 7.6445 \times 10^{-8} \exp(25.36 y^{2.469}) - 8.4410 \times 10^{-8} \exp(25.262 y^{2.478})$

$$j_n = \frac{I}{F} = \frac{i_0}{F} \left( \exp\left(\frac{\alpha_a F}{RT} \eta\right) - \exp\left(-\frac{\alpha_c F}{RT} \eta\right) \right) \quad (7)$$

where,  $\eta$ , is the surface overpotential defined as:

$$\eta = U - \phi_1 - \phi_2 \quad (8)$$

And  $i_0$  is the exchange current density defined as [9]:

$$i_0 = Fk_0(c_{2s})^\alpha (C_{max} - C_{1s})^\alpha C_{1s}^\alpha \quad (9)$$

where,  $k_0$  is a reaction rate constant,  $C_{1s}$  and  $C_{2s}$  are the lithium ion concentration at the interface of the active material and electrolyte, respectively,  $C_{max}$  is the maximum concentration of lithium inside the solid matrix, and  $U$  is the open circuit potential which is a function of  $C_{1s}$ .

#### 4.3. Governing equations in microscale and bridging

The conservation of mass inside the microscale is governed by Fick's mass transfer equation:

$$\frac{\partial c_1}{\partial t} = \nabla \cdot (D_1 \nabla c_1) \quad (10)$$

where,  $c_1$  is the concentration of lithium ion inside the microstructure,  $D_1$  is the solid state diffusivity of LFP, and  $\nabla$  operator applies on the spatial coordinate in the 3D microscale domain. Boundary condition for the eq. (11) is expressed as:

$$j_n = -D_1 \nabla c_1 \cdot n \quad \text{at the interface of the solid matrix and electrolyte} \quad (11)$$

where,  $n$  is the unit vector normal to the boundary interface and  $j_n$  is the pore-wall flux imported from macroscale. As shown in Fig. 2, bridging between two scales is a circular or two way coupling of state variables in real time (concurrent coupling). Fig. 2 shows the multiscale framework along with the time dependent solution algorithm in counter clock wise direction. The marching in time starts by calculating pore-wall flux,  $j_n$  from macroscale initial values, shown by red (in the web version) bubble in Fig. 2. The calculated pore-wall flux,  $j_n$  then is used as the boundary condition (eq. (11)) for eq. (10) in microscale; by this lithium in concentration,

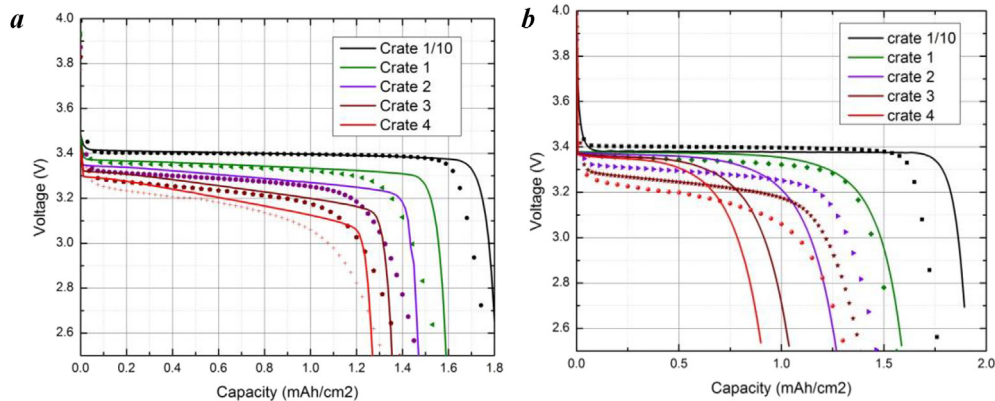


**Fig. 3.** Comparison of the modeling (line) and experimental (dots) results for an LFP electrode half-cell at different discharge rates (a) multiscale model (b) Newman P2D model.



macroscale governing equations. This loop continues until the stop operation condition of the cell is satisfied.

The only remaining issue to complete the model development is determining solid state diffusivity ( $D_1$ ) of LFP, where special care needs to be taken. In modeling LIBs, all chemistries share a common modeling framework that involves transport of charge across both the electronic and ionic phases in an electrode, transport of mass in the ionic phase, reaction at the electrode/electrolyte interface, and transport of Li ions in the solid particles [50]. The unique features of each chemistry are then accounted for by changing the parameters

that describe these processes e.g. thermodynamic potential and diffusion coefficient appropriately. However, the LFP electrode differs from these systems in that it undergoes a phase change with the lithiated and unlithiated forms having distinct phases, as evidenced from X-ray diffraction patterns of the material at various stages of lithiation [51]. The phase change of LFP first was incorporated into P2D model using the shrinking core concept by Srinivasan et al. [50]. The core–shell model considers the existence of a core of one phase covered with a shell of the second phase and transport of lithium ions in the shell move the boundary between

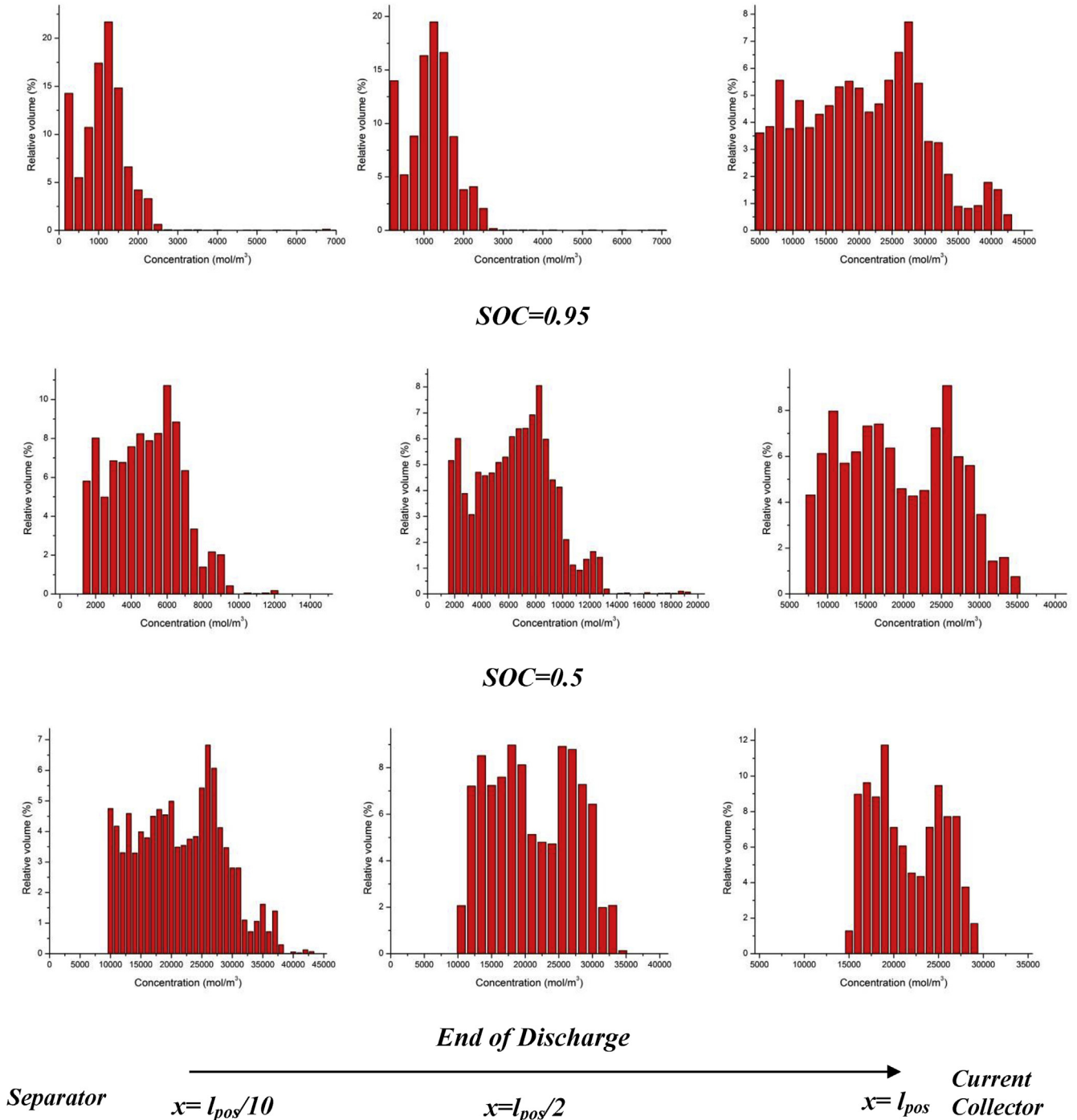


Fig. 5. Histograms of the lithium ion concentration inside microstructure using multiscale model at c-rate = 1.

two phases. The validity of the Core-Shell model has been controversial [52–54] since it has shown to be incompatible with experimental observation [55]. To account for phase change, here we have used the variable solid-state diffusivity model [44,52,54] which model LFP phase change by a thermodynamic factor  $\gamma$  as:

$$\gamma = -\frac{F}{RT}y(1-y)\frac{\partial U}{\partial y} \tag{13}$$

$$D_1 = D_{LFP}\gamma \tag{12}$$

$\gamma$  can be calculated based on the open circuit potential  $U$ , and state of charge of the electrode,  $y$ , using:

### 5. Results and discussion

As discussed earlier, in the P2D model it is assumed that the porous electrode consists of isotropic, homogeneous, mono-dispersed spherical particles [27]. These assumptions are not valid for real battery electrodes where the electrode microstructure is

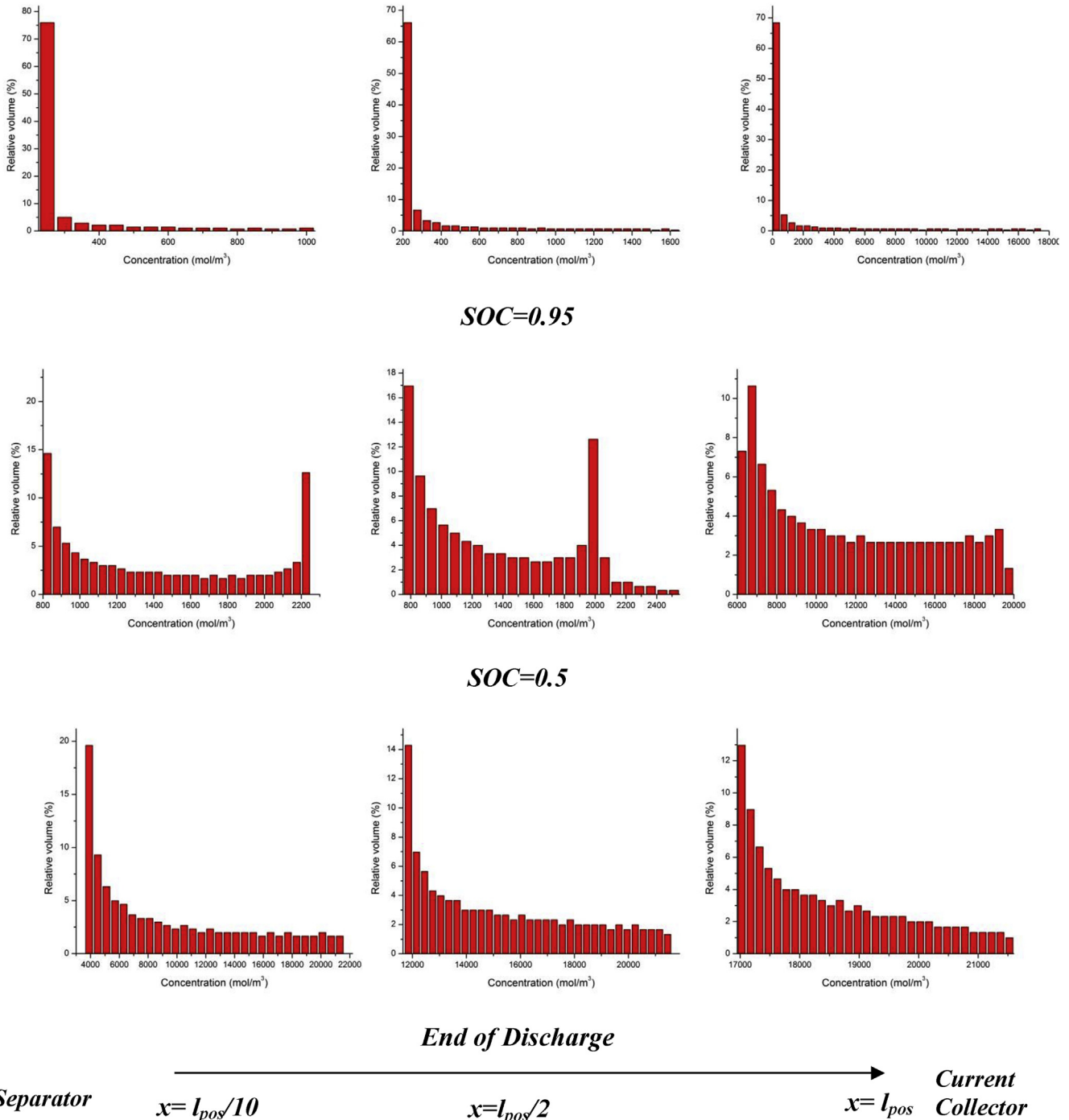


Fig. 6. Histogram of the lithium ion concentration using P2D model inside spherical particles with radius of 72 nm at c-rate = 1.

inhomogeneous, non-isotropic with 3D pores and constructed from different size and shape particles. In this study, consideration of the 3D reconstructed real electrode microstructure creates the opportunity to remove the P2D assumptions to reach more accurate and more detailed results related to the electrode microstructure.

The galvanostatic discharge at various rates for an LFP half-cell with the model parameters listed in Table 3 is obtained from the multiscale model and shown in Fig. 3a. It is noted that the multiscale model takes the real electrode structure into account. The design adjustable parameters including the solid phase diffusion

coefficient,  $D_{LFP}$  and solid matrix conductivity,  $\sigma$ , are determined based on the method described in Ref. [50] and compared with the obtained experimental data. In addition, to compare the multiscale model with Newman P2D model, the half-cell is also simulated based on the P2D model and results are shown in Fig. 3b. In P2D model, the average spherical particle diameter was chosen to be 37 nm based on the single particle distribution obtained by SEM (see Fig. 1c) [44]. The specific surface area of electrode/electrolyte in the P2D model is calculated for spherical particles with radius of 37 nm and the effective transport properties including  $D_{eff}$ ,  $k_{eff}$ ,  $\sigma_{eff}$ ,

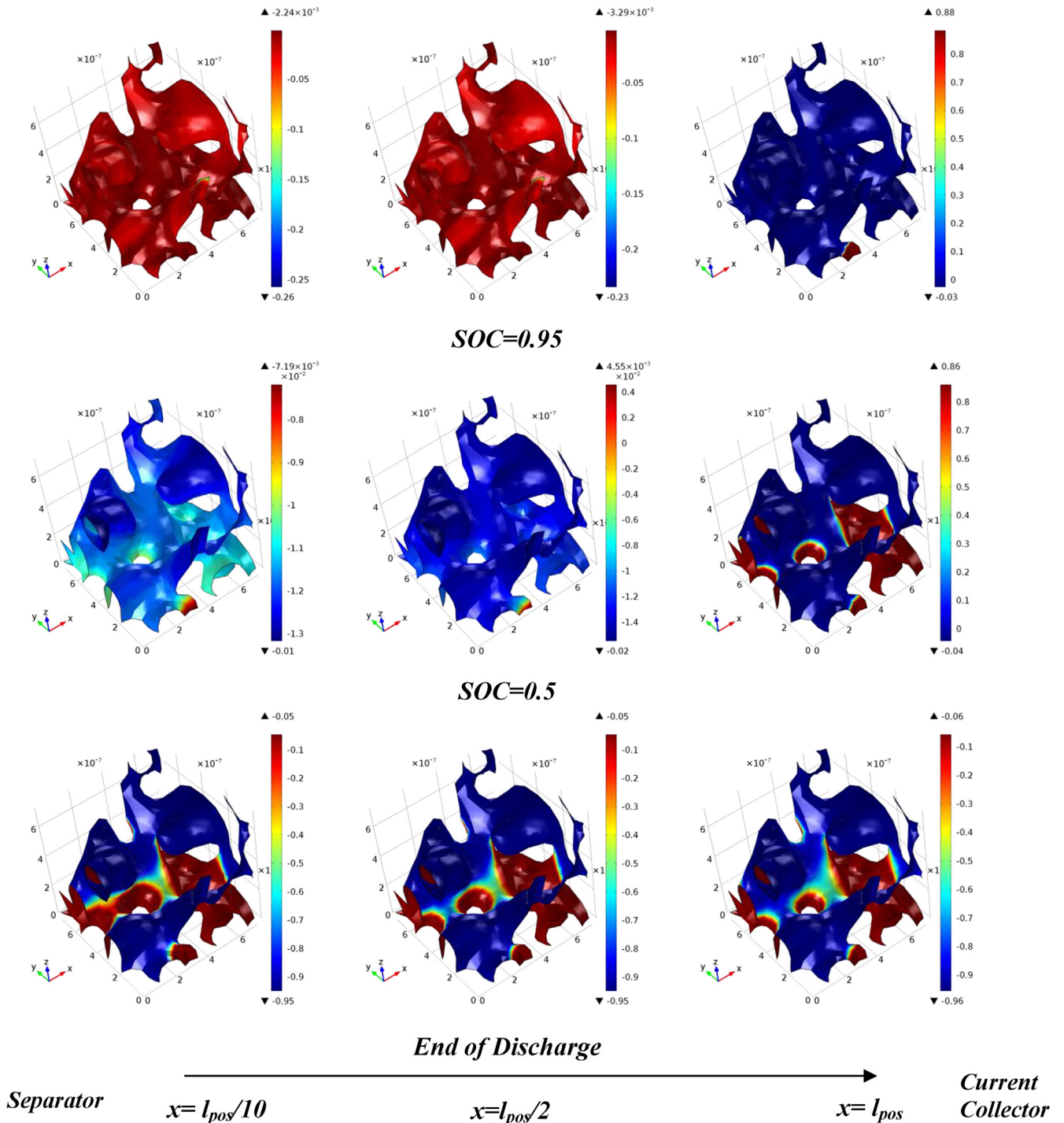


Fig. 7. Distribution of the overpotential (unit:V) on the solid/electrolyte interface during discharge at c-rate = 1 for different SOCs.

are calculated using Bruggeman relationship with the coefficient of 1.5 [9]. As shown in Fig. 3b, the P2D model over predicts the capacity at discharge rates lower than 1 and under predicts the capacity for higher discharge rates. Other researchers have also achieved the same results for the Newman P2D model [44,50,52]. In the modeling work using P2D model, normal remedy to address this issue is using two [50] or four [44,52] different particle sizes to mimic the real electrode microstructure. On the other hand, the multiscale model could also predict the discharge curves at

different rates without further assumption using real electrode morphology. The real electrode geometry provides higher surface area for the lithium to intercalate compared to the spherical particle geometry with average size in the P2D. Moreover, the multi-scale model does not use the Bruggeman relation to calculate the effective transport properties.

Even though P2D model has proven successful to predict the performance, it fails to predict the degradation and failure. The main advantage using tomographic data in the current work is to

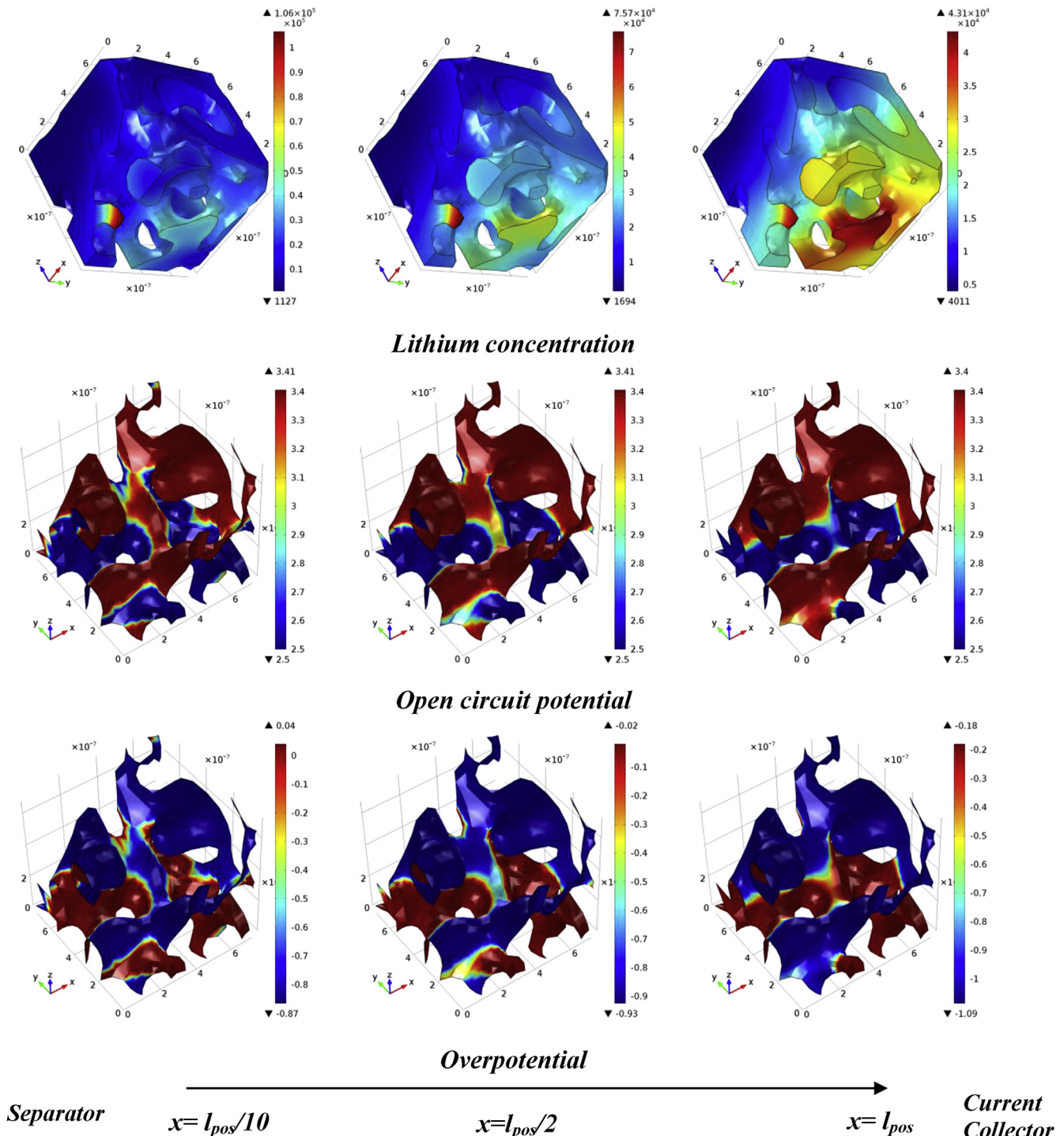


Fig. 8. Distribution of lithium concentration ( $\text{mol m}^{-3}$ ) and Interfacial properties along the electrode thickness direction at the end of discharge for c-rate = 4.

visualize the heterogeneities inside the electrode microstructure contributing to electrode failure and degradation. The approach used in this study can provide valuable insight into the spatial distribution of electrochemical properties inside the electrode structure. For the LFP half-cell, during discharge at 1 C, the lithium concentration, current density, open circuit potential (OCP), overpotentials, and intercalation reaction rate are determined from the multiscale modeling. The lithium concentration in the electrode microstructure along the electrode thickness direction at discharge rate of unity for various states of charges (SOCs) is shown in Fig. 4. The average lithium ion concentration increases from the separator toward the current collector. Moreover, lithium ion concentration in microstructure is much higher in the region with smaller cross section area perpendicular to lithium intercalation pathway. At SOC = 0.5, the maximum lithium ion concentration is  $4.51 \times 10^4$  mol/m<sup>3</sup> which is in the location of one of those sharp regions close to the current collector (cal. around 10 times compared to average lithium ion concentration in the REV). Moreover, Fig. 4 shows that sharp region at SOC = 0.95, have higher concentration than the maximum concentration at the end of discharge ( $4.51 \times 10^4$  compared to  $2.9 \times 10^4$ ). The last feature that can be found from the concentration distribution is that the maximum concentration occurs in different locations across the electrode thickness at different times. The maximum concentration takes place in the cathode current collector location at SOC = 0.95 and 0.5, whereas, it occurs in the location close to the separator at the end of discharge.

These unpredictable behavior confirms the inherent non-homogenous microstructure of LIB and could not be detected using homogenized methods. This behavior could be described better by comparing the lithium ion concentration histogram as shown in Fig. 5. The distribution range of lithium concentration becomes wider from separator to current collector for SOC = 0.95 and 0.5. This would result in the more inhomogeneity in concentration for the particles closer to current collector. However, at the end of discharge the condition is reversed and the inhomogeneity shifts toward the separator. To emphasize the model capability to capture inhomogeneity, lithium ion concentration result using P2D is also shown in Fig. 6 for comparison. The wider range of lithium concentration using multiscale model is evident comparing two Figs. 5 and 6. In addition, lithium concentration distribution using P2D model shows a certain trend because the properties vary in direction of electrode thickness. Nevertheless, the property distribution based on the real microstructure properties show no clear trend due to inherent inhomogeneity of microstructures.

Fig. 7 illustrates the overpotential distribution on the electrode solid/electrolyte interface. The overpotential is calculated using eq. (8), and is a function of OCP, electric potential in the solid,  $\phi_1$ , and electric potential in electrolyte,  $\phi_2$ . OCP is obtained by microscale simulation results from the lithium concentration on the solid/electrolyte interface (see Fig. S3). The OCP is the function of the SOC on the electrode solid/electrolyte interface based on the experimental data obtained during the half-cell discharge at C/50 (shown in Table 3). Inhomogeneous distribution of the OCP is due to different lithium concentrations and material utilization during discharge. On the other hand, electric and electronic potentials are

achieved through macroscale results. Therefore, the overpotential is a property that requires to be calculated using results from the multiscale: microscale and macroscale. On the solid/electrolyte interface at a certain point along the thickness direction, the overpotential variations is primary due to OCP changes. However, among different location along thickness direction is due to different contributions of OCP and electric potential in the solid and electrolyte.

To compare the simulation results at different rates, discharge process at c-rate = 4 is presented in Fig. 8. Lithium ion concentration in the electrode microstructure at the end of discharge for c-rate = 4 is shown in the first row in Fig. 8. Simulation results show higher inhomogeneity inside microstructure at c-rate = 4 (1st row in Fig. 8) compared to the c-rate = 1 (3rd row of Fig. 4). The inhomogeneity could be better scrutinized by comparing the range of lithium concentration at different rates. Table 4 summarizes those ranges which clearly confirms the wider range of concentration at higher rate due to effect of inhomogeneities. In addition, OCP and overpotential interfacial properties at the solid/electrolyte interface along the electrode thickness direction are also shown in 2nd and 3rd row of Fig. 8, respectively. Fig. 8 shows that the interfacial properties are also distributed in a wider range at c-rate = 4 compared to c-rate = 1. Histogram graph of lithium concentration and interfacial properties using multiscale model at c-rate = 4 along electrode thickness direction is presented in Fig. S4. For comparison histogram graph of lithium concentration using P2D model is also shown in Fig. S5 which clearly shows the wider range of properties distribution at higher rate.

## 6. Conclusions

We have successfully established an imaged-based multiscale model to study the real microstructure of electrodes of lithium ion batteries. The model is based on the real 3D microstructure data, while take advantage of the traditional homogenous 1D model in macroscale to characterize discharge/charge performance. In macroscale, the model is modified through dropping Bruggeman relation and replacing it by real tortuosity of the electrode porous structure. In addition, the interfacial surface area is determined based on the nano-XCT data removing the typical relation assuming spherical particles. The coupling between micro and macro scales are performed in real time unlike using common surrogate based models for microscale. The simulation results could predict the experimental discharge voltage of LFP cathodes at different rates. The simulation showed that the lithium ion concentration in the electrode active material structure is much higher in the region with smaller cross-section area perpendicular to the lithium intercalation pathway. Such low area regions would intercalate ca. 10 times higher than the area with an average concentration. The approach used in this study can provide valuable insight into the spatial distribution of lithium ions inside the microstructure of LIB electrodes. The inhomogenous microstructure of LFP causes a wide range of physical and electrochemical properties compared to the homogenous model.

## Acknowledgments

A.G.K. thanks Hey Woong Park for helpful hints and fruitful discussions. This research was supported by the Natural Sciences and Engineering Research Council of Canada (NSERC) through grants to Z.C. and the University of Waterloo. The research was also supported by the University of Akron.

**Table 4**

Lithium concentration range in the microstructure along the electrode thickness direction at different rates (time: end of discharge, unit: mol/m<sup>3</sup>).

C-rate	$l_{pos/10}$	$l_{pos/2}$	$l_{pos}$
1	$3.50 \times 10^4$	$2.33 \times 10^4$	$1.37 \times 10^4$
4	$1.05 \times 10^5$	$7.40 \times 10^4$	$3.91 \times 10^4$

## Appendix A. Supplementary data

Supplementary data related to this article can be found at <http://dx.doi.org/10.1016/j.jpowsour.2015.12.134>.

## Nomenclature

a	specific interfacial area ( $\text{m}^2/\text{m}^3$ )
c	concentration of electrolyte ( $\text{mol m}^{-3}$ )
D	diffusion coefficient ( $\text{m}^2 \text{s}^{-1}$ )
f	mean molar activity coefficient
F	Faraday's constant, $96487 \text{ (C mol}^{-1}\text{)}$
i	current density ( $\text{A m}^{-2}$ )
I	total applied current density to the cell ( $\text{A m}^{-2}$ )
$j_n$	pore-solid flux of lithium ions ( $\text{mol}/(\text{m}^3 \text{s})$ )
$k_0$	reaction rate constant ( $\text{mol m}^{-2}\text{s}^{-1}(\text{mol m}^{-3})^{-1.5}$ )
l	thickness (m)
n	unit vector normal to the boundary interface
OCP	interfacial open circuit potential (V)
R	universal gas constant ( $\text{J}/(\text{mol. K})$ )
t	time (s)
T	temperature (K)
$t_+$	transference number of lithium-ion with respect to the solvent
U	Open circuit potential of LFP (V)
x	spatial coordinate along the thickness of the cell

## Greek letters

$\alpha$	apparent transfer coefficient (kinetic parameter)
$\gamma$	thermodynamic factor for variable solid state diffusivity model
$\varepsilon$	porosity
$\kappa$	electrolyte conductivity ( $\text{S m}^{-1}$ )
$\sigma$	conductivity of solid matrix ( $\text{S m}^{-1}$ )
$\phi$	electric potential (V)
$\tau$	electrode tortuosity
$\eta$	surface overpotential (V)

## Subscripts

1	Solid phase
2	electrolyte phase
a	anodic
c	cathodic
eff	effective
ini	initial
LFP	lithium iron phosphate
max	maximum
s	solid/electrolyte interface
sep	separator
pos	positive electrode

## References

- J.B. Dunn, L. Gaines, J.C. Kelly, C. James, K.G. Gallagher, The significance of Li-ion batteries in electric vehicle life-cycle energy and emissions and recycling's role in its reduction, *Energy Environ. Sci.* 8 (2014) 158–168, <http://dx.doi.org/10.1039/C4EE03029J>.
- E. Samadani, M. Mastali, S. Farhad, R.A. Fraser, M. Fowler, Li-ion battery performance and degradation in electric vehicles under different usage scenarios, *Int. J. Energy Res.* 31 (2015) 135–147, <http://dx.doi.org/10.1002/er.3378>.
- X. Li, D. Luo, X. Zhang, Z. Zhang, Enhancement of electrochemical performances for LiFePO<sub>4</sub>/C with 3D-grape-bunch structure and selection of suitable equivalent circuit for fitting EIS results, *J. Power Sources* 291 (2015) 75–84, <http://dx.doi.org/10.1016/j.jpowsour.2015.05.018>.
- Y. Honda, S. Muto, K. Tatsumi, H. Kondo, K. Horibuchi, T. Kobayashi, et al., Microscopic mechanism of path-dependence on charge–discharge history in lithium iron phosphate cathode analysis using scanning transmission electron microscopy and electron energy-loss spectroscopy spectral imaging, *J. Power Sources* 291 (2015) 85–94, <http://dx.doi.org/10.1016/j.jpowsour.2015.04.183>.
- S.J. Dillon, K. Sun, Microstructural design considerations for Li-ion battery systems, *Curr. Opin. Solid State Mater. Sci.* 16 (2012) 153–162, <http://dx.doi.org/10.1016/j.cossms.2012.03.002>.
- K.M.O. Jensen, X. Yang, J.V. Laveda, W.G. Zeier, K.A. See, M.D. Michiel, et al., X-ray diffraction computed tomography for structural analysis of electrode materials in batteries, *J. Electrochem. Soc.* 162 (2015) A1310–A1314, <http://dx.doi.org/10.1149/2.0771507jes>.
- F. Tariq, V. Yufit, M. Kishimoto, P.R. Shearing, S. Menkin, D. Golodnitsky, et al., Three-dimensional high resolution X-ray imaging and quantification of lithium ion battery mesocarbon microbead anodes, *J. Power Sources* 248 (2014) 1014–1020, <http://dx.doi.org/10.1016/j.jpowsour.2013.08.147>.
- M. Ebner, F. Geldmacher, F. Marone, M. Stampanoni, V. Wood, X-ray tomography of porous, transition metal oxide based lithium ion battery electrodes, *Adv. Energy Mater.* 3 (2013) 845–850, <http://dx.doi.org/10.1002/aenm.201200932>.
- M. Doyle, J. Newman, The use of mathematical modeling in the design of lithium/polymer battery systems, *Electrochim. Acta* 40 (1995) 2191–2196, [http://dx.doi.org/10.1016/0013-4686\(95\)00162-8](http://dx.doi.org/10.1016/0013-4686(95)00162-8).
- T.F. Fuller, M. Doyle, J. Newman, Technical Papers Electrochemical Science and Technology. Simulation and Optimization of the Dual Lithium Ion Insertion Cell, 141 (1994).
- W.B. Gu, B.Y. Wang, C.Y. Gu, W.B. Liaw, Micro-macroscopic coupled modeling of batteries and fuel cells, *J. Electrochem. Soc.* 145 (1998) 3418, <http://dx.doi.org/10.1149/1.1838821>.
- V. Chabot, S. Farhad, Z. Chen, A.S. Fung, A. Yu, F. Hamdullahpur, Effect of electrode physical and chemical properties on lithium-ion battery performance, *Int. J. Energy Res.* 31 (2007) 135–147 doi: 10.1002/er.
- W.B. Gu, C.Y. Wang, J.W. Weidner, R.G. Jungst, G. Nagasubramanian, Computational fluid dynamics modeling of a lithium/thionyl chloride battery with electrolyte flow, *J. Electrochem. Soc.* 147 (2000) 427, <http://dx.doi.org/10.1149/1.1393213>.
- H. Zarrin, S. Farhad, F. Hamdullahpur, V. Chabot, A. Yu, M. Fowler, et al., Effects of diffusive charge transfer and salt concentration gradient in electrolyte on Li-ion battery energy and power densities, *Electrochim. Acta* 125 (2014) 117–123, <http://dx.doi.org/10.1016/j.electacta.2014.01.022>.
- M.F.M.M. Majdabadi Kohneh, E. Samadani, S. Farhad, R. Fraser, Three-dimensional electrochemical analysis of a graphite/LiFePO<sub>4</sub> Li-ion cell to improve its durability, *SAE Tech. Pap.* (2015), <http://dx.doi.org/10.4271/2015-01-1182>.
- V. Ramadesigan, P.W.C. Northrop, S. De, S. Santhanagopalan, R.D. Braatz, V.R. Subramanian, Modeling and simulation of lithium-ion batteries from a systems engineering perspective, *J. Electrochem. Soc.* 159 (2012) R31–R45, <http://dx.doi.org/10.1149/2.018203jes>.
- R. Fu, S. Choe, V. Agubra, J. Fergus, Development of a physics-based degradation model for lithium ion polymer batteries considering side reactions, *J. Power Sources* 278 (2015) 506–521, <http://dx.doi.org/10.1016/j.jpowsour.2014.12.059>.
- C.H. Lee, S.J. Bae, M. Jang, A study on effect of lithium ion battery design variables upon features of thermal-runaway using mathematical model and simulation, *J. Power Sources* 293 (2015) 498–510, <http://dx.doi.org/10.1016/j.jpowsour.2015.05.095>.
- R. Zhao, J. Liu, J. Gu, The effects of electrode thickness on the electrochemical and thermal characteristics of lithium ion battery, *Appl. Energy* 139 (2015) 220–229, <http://dx.doi.org/10.1016/j.apenergy.2014.11.051>.
- C.-W. Wang, A.M. Sastry, Mesoscale modeling of a Li-ion polymer cell, *J. Electrochem. Soc.* 154 (2007) A1035, <http://dx.doi.org/10.1149/1.2778285>.
- A. Gupta, J.H. Seo, X. Zhang, W. Du, A.M. Sastry, W. Shyy, Effective transport properties of LiMn<sub>2</sub>O<sub>4</sub> electrode via particle-scale modeling, *J. Electrochem. Soc.* 158 (2011) A487, <http://dx.doi.org/10.1149/1.3560441>.
- D. Kehrwald, P.P.R. Shearing, N.P.N. Brandon, P.K.P. Sinha, S.J.S. Harris, Local tortuosity inhomogeneities in a lithium battery composite electrode, *J. Electrochem. Soc.* 158 (2011) A1393, <http://dx.doi.org/10.1149/2.079112jes>.
- D.-W. Chung, M. Ebner, D.R. Ely, V. Wood, R. Edwin García, Validity of the Bruggeman relation for porous electrodes, *Model. Simul. Mater. Sci. Eng.* 21 (2013) 074009, <http://dx.doi.org/10.1088/0965-0393/21/7/074009>.
- G.B. Less, J.H. Seo, S. Han, A.M. Sastry, J. Zausch, A. Latz, et al., Micro-scale modeling of Li-ion batteries: parameterization and validation, *J. Electrochem. Soc.* 159 (2012) A697, <http://dx.doi.org/10.1149/2.096205jes>.
- M. Ebner, F. Marone, M. Stampanoni, V. Wood, Visualization and quantification of electrochemical and mechanical degradation in Li ion batteries, *Science* 342 (2013) 716–720, <http://dx.doi.org/10.1126/science.1241882>.
- C. Lim, B. Yan, L. Yin, L. Zhu, Simulation of diffusion-induced stress using reconstructed electrodes particle structures generated by micro/nano-CT, *Electrochim. Acta* 75 (2012) 279–287.
- B. Yan, C. Lim, L. Yin, L. Zhu, Three dimensional simulation of galvanostatic discharge of LiCoO<sub>2</sub> cathode based on X-ray nano-CT images, *J. Electrochem. Soc.* 159 (2012) A1604–A1614, <http://dx.doi.org/10.1149/2.024210jes>.
- B. Yan, C. Lim, L. Yin, L. Zhu, Simulation of heat generation in a reconstructed LiCoO<sub>2</sub> cathode during galvanostatic discharge, *Electrochim. Acta* 100 (2013) 171–179, <http://dx.doi.org/10.1016/j.electacta.2013.03.132>.
- D.-W. Chung, P.R. Shearing, N.P. Brandon, S.J. Harris, R.E. García, R.E. García, Particle size polydispersity in Li-ion batteries, *J. Electrochem. Soc.* 161 (2014) A422–A430, <http://dx.doi.org/10.1149/2.097403jes>.
- A.A. Franco, Multiscale modelling and numerical simulation of rechargeable

- lithium ion batteries: concepts, methods and challenges, RSC Adv. 3 (2013) 13027–13058, <http://dx.doi.org/10.1039/c3ra23502e>.
- [31] X. Zhang, A.M. Sastry, W. Shyy, Intercalation-induced stress and heat generation within single lithium-ion battery cathode particles, J. Electrochem. Soc. 155 (2008) A542, <http://dx.doi.org/10.1149/1.2926617>.
- [32] L. Zielke, T. Hutzenlaub, D.R. Wheeler, C.-W. Chao, I. Manke, A. Hilger, et al., Three-phase multiscale modeling of a LiCoO<sub>2</sub> cathode: combining the advantages of FIB-SEM imaging and X-ray tomography, Adv. Energy Mater. (2014), <http://dx.doi.org/10.1002/aenm.201401612> n/a–n/a.
- [33] G. Richardson, G. Denuault, C.P. Please, Multiscale modelling and analysis of lithium-ion battery charge and discharge, J. Eng. Math. 72 (2012) 41–72, <http://dx.doi.org/10.1007/s10665-011-9461-9>.
- [34] X. Zhang, Multiscale Modeling of Li-ion Cells: Mechanics, Heat Generation and Electrochemical Kinetics, 2009, pp. 1–178.
- [35] L. Tan, N. Zabarar, Multiscale modeling of alloy solidification using a database approach, J. Comput. Phys. 227 (2007) 728–754, <http://dx.doi.org/10.1016/j.jcp.2007.08.016>.
- [36] N.V. Queipo, R.T. Haftka, W. Shyy, T. Goel, R. Vaidyanathan, P. Kevin Tucker, Surrogate-based analysis and optimization, Prog. Aerosp. Sci. 41 (2005) 1–28, <http://dx.doi.org/10.1016/j.paerosci.2005.02.001>.
- [37] W. Du, N. Xue, W. Shyy, J.R.R.A. Martins, A surrogate-based multi-scale model for mass transport and electrochemical kinetics in lithium-ion battery electrodes, J. Electrochem. Soc. 161 (2014) E3086–E3096, <http://dx.doi.org/10.1149/2.013408jes>.
- [38] X-ray Computed Tomography Facility, (n.d.). <http://www.cmu.edu/me/xctf/>.
- [39] S. Komini, A. Mohamed, J. Whitacre, Multiple imaging mode X-ray computed tomography for distinguishing carbon additives in lithium battery cathodes, J. Power Sources 283 (2015) 1–16, <http://dx.doi.org/10.1016/j.jpowsour.2015.02.086>.
- [40] G. Liu, H. Zheng, X. Song, V.S. Battaglia, Particles and polymer binder interaction: a controlling factor in lithium-ion electrode performance, J. Electrochem. Soc. 159 (2012) A214, <http://dx.doi.org/10.1149/2.024203jes>.
- [41] M. Gnanavel, M.U.M. Patel, A.K. Sood, A.J. Bhattacharyya, High rate capability lithium iron phosphate wired by carbon nanotubes and galvanostatic transformed to graphitic carbon, J. Electrochem. Soc. 159 (2012) A336, <http://dx.doi.org/10.1149/2.015204jes>.
- [42] M. Safari, C. Delacourt, Mathematical modeling of lithium iron phosphate electrode: galvanostatic charge/discharge and path dependence, J. Electrochem. Soc. 158 (2011) A63, <http://dx.doi.org/10.1149/1.3515902>.
- [43] W. Shyy, S.S. Thakur, H. Ouyang, J. Liu, E. Bloch, Computational techniques for complex transport phenomena, 1997. doi: 10.1017/CBO9780511665462.
- [44] M. Mastali Majdabadi, S. Farhad, M. Farkhondeh, R.A. Fraser, M. Fowler, Simplified electrochemical multi-particle model for LiFePO<sub>4</sub> cathodes in lithium-ion batteries, J. Power Sources 275 (2015) 633–643, <http://dx.doi.org/10.1016/j.jpowsour.2014.11.066>.
- [45] A. Ghorbani, S. Farhad, V. Chabot, A. Yu, Z. Chen, Effects of structural design on the performance of electrical double layer capacitors, Appl. Energy 138 (2015) 631–639, <http://dx.doi.org/10.1016/j.apenergy.2014.09.033>.
- [46] A.G. Kashkooli, S. Farhad, A.S. Fung, Z. Chen, Effect of convective mass transfer on lead-acid battery performance, Electrochim. Acta 97 (2013) 278–288, <http://dx.doi.org/10.1016/j.electacta.2013.02.116>.
- [47] J. Newman, W. Tiedemann, Porous-electrode theory with battery applications, AIChE J. 21 (1975) 25–41, <http://dx.doi.org/10.1002/aic.690210103>.
- [48] S.J. Cooper, D.S. Eastwood, J. Gelb, G. Damblanc, D.J.L. Brett, R.S. Bradley, et al., Image based modelling of microstructural heterogeneity in LiFePO<sub>4</sub> electrodes for Li-ion batteries, J. Power Sources 247 (2014) 1033–1039, <http://dx.doi.org/10.1016/j.jpowsour.2013.04.156>.
- [49] M. Doyle, Modeling of galvanostatic charge and discharge of the lithium/polymer/insertion cell, J. Electrochem. Soc. 140 (1993) 1526, <http://dx.doi.org/10.1149/1.2221597>.
- [50] V. Srinivasan, J. Newman, Discharge model for the lithium iron-phosphate electrode, J. Electrochem. Soc. 151 (2004) A1517, <http://dx.doi.org/10.1149/1.1785012>.
- [51] A. Yamada, Y. Kudo, K.-Y. Liu, Phase diagram of Li<sub>x</sub>(Mn<sub>y</sub>)Fe<sub>1-y</sub>PO<sub>4</sub> (0 ≤ x, y ≤ 1), J. Electrochem. Soc. 148 (2001) A1153, <http://dx.doi.org/10.1149/1.1401083>.
- [52] M. Farkhondeh, M. Safari, M. Pritzker, M. Fowler, T. Han, J. Wang, et al., Full-range simulation of a commercial LiFePO<sub>4</sub> electrode accounting for bulk and surface effects: a comparative analysis, J. Electrochem. Soc. 161 (2013) A201–A212, <http://dx.doi.org/10.1149/2.094401jes>.
- [53] M. Farkhondeh, M. Pritzker, M. Fowler, M. Safari, C. Delacourt, Mesoscopic modeling of Li insertion in phase-separating electrode materials: application to lithium iron phosphate, Phys. Chem. Chem. Phys. 16 (2014) 22555–22565, <http://dx.doi.org/10.1039/C4CP03530E>.
- [54] M. Safari, M. Farkhondeh, M. Pritzker, M. Fowler, T. Han, S.K. Chen, Simulation of lithium iron phosphate lithiation/delithiation: limitations of the core-shell model, Electrochim. Acta 115 (2014) 352–357, <http://dx.doi.org/10.1016/j.electacta.2013.10.159>.
- [55] C. Delmas, M. Maccario, L. Croguennec, F. Le Cras, F. Weill, Lithium deintercalation in LiFePO<sub>4</sub> nanoparticles via a domino-cascade model, Nat. Mater. 7 (2008) 665–671, <http://dx.doi.org/10.1038/nmat2230>.